




Database of Martian dust optical properties in the UV-vis-NIR

Julia Martikainen ¹★, Olga Muñoz ¹, Juan Carlos Gómez Martín,¹ María Passas Varo,¹ Teresa Jardiel,² Marco Peiteado,² Yannick Willame,³ Lori Neary,³ Tim Becker⁴ and Gerhard Wurm ⁴

¹*Instituto de Astrofísica de Andalucía, CSIC, 18008 Granada, Spain*

²*Instituto de Cerámica y Vidrio, CSIC, 28049 Madrid, Spain*

³*Belgian Institute for Space Aeronomy (IASB-BIRA), 1180 Brussels, Belgium*

⁴*University of Duisburg-Essen, Faculty of Physics, 47057 Duisburg, Germany*

Accepted 2025 January 14. Received 2025 January 14; in original form 2024 October 22

ABSTRACT

The experimental data base of scattering matrices of three well-characterized Martian dust analogues with narrow particle size distributions representative of Martian dust aerosols is used to check the suitability of hexahedra model particles to reproduce the scattering behaviour of realistic polydisperse irregular particles at 488 and 640 nm. In general, the hexahedra model performs well. The scattering matrix elements as functions of the scattering angle can be reproduced with good accuracy for particle size distributions that contain small particles; however, the discrepancies increase with increasing particle size due to wavelength-scale surface roughness and internal structure found within large dust grains that are not accounted for by the smooth hexahedra model particles. We further perform sensitivity tests to study the effect of absorption, real part of the complex refractive index, and particle size distribution within the model to understand their contribution to the modelled scattering matrix elements. By using the best-fitting parameters from the sensitivity study, we have created a data base of optical properties that includes bulk extinction efficiencies, single-scattering albedos, asymmetry factors, extinction cross-sections, and phase matrices of the analogue samples from 200 to 2000 nm. The obtained values can be further used in radiative-transfer simulations. This work emphasizes the importance of accounting for the full scattering matrix as information on particle shape, size, and complex refractive index is lost when omitting polarization.

Key words: scattering – methods: numerical – planets and satellites: terrestrial planets.

1 INTRODUCTION

Airborne dust is a major driver of the Martian atmosphere, affecting temperature, near-surface climate, and global circulation. In most radiative-transfer codes, the scattering effect is simulated using only the phase function, i.e. using only one element of the scattering matrix. The phase function of Martian dust particles is often derived by Mie theory for spherical particles or assuming analytical Henyey–Greenstein phase functions. A significant step forward in reproducing non-sphericity of Martian dust was suggested by Wolff et al. (2006), with a cylinder model. Even so, as pointed out by Wolff et al. (2010), the calculated phase functions for a size distribution of cylinders produce a considerable overestimation of the phase function near backscattering direction when comparing with observation of Martian dust (Tomasko et al. 1999). However, that overestimation is not observed when the phase function of natural dust particles is experimentally obtained in the laboratory. It has been shown that the use of too simplistic particle shapes in scattering models can cause significant errors in the retrieved optical thicknesses of irregular mineral dust (Mishchenko et al. 2003). Furthermore, retrieving optical properties from observations is challenging due to

several unknown parameters, such as the particle size distribution, that cannot be directly measured at the time of the observations and significantly influence the retrievals.

In this study, we utilize a unique experimental data base of scattering matrices of the JSC Mars-1, MGS-1, and MMS-2 Martian dust analogues obtained in the laboratory (Martikainen et al. 2024) to check the validity of state-of-the-art numerical techniques based on simplified model particles to reproduce the scattering behaviour of realistic polydisperse irregular particles. Initially, several advanced single-scattering data bases were considered for our modelling purposes, however, the single-scattering property data base of hexahedra model particles (Saito et al. 2021) was superior for reproducing experimental data and was therefore selected. As the particle size distributions and the imaginary parts of the complex refractive indices are known through measurements and previous studies (see Martikainen et al. 2023, 2024), free parameters within the model are limited and can be efficiently tested. Once the model is validated on experimental data, it is then used for computations of other optical properties of the particles or wavelengths for which experiments are highly difficult or not possible at all, such as cross-sections, single-scattering albedos, extinction efficiencies, asymmetry factors, and phase matrices. The combination of computational and experimental data can create synergy to the benefit of each of them. This creates more insight, data and useful ideas that cannot be obtained from

* E-mail: juliamar@iaa.es

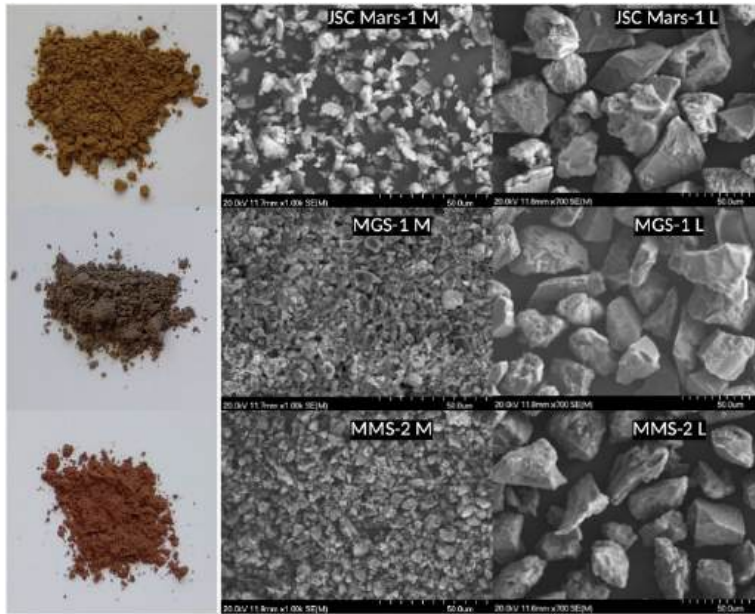


Figure 1. The pictures of the JSC Mars-1 (top), MGS-1 (middle), and MMS-2 (bottom) analogues together with the SEM images of their L and M size fractions. The ruler intervals on the bottom right of the SEM images are 5 μm .

computational means alone. Thus, combination of experimental measurements with powerful simulation methods is the ideal scenario to characterize the scattering properties of Martian dust particles. This study provides a computed data base of optical properties of three Martian dust analogues with narrow particle size distributions for a wavelength range of 200–2000 nm using the experimentally validated model.

The paper is organized as follows. In Section 2, we introduce the analogue samples, whereas the experimental scattering matrices are presented in Section 3. The methodology of modelling the measurements is explained in Section 4. The results are presented and discussed in Section 5, and the concluding remarks are given in Section 6.

2 THE ANALOGUE SAMPLES

2.1 Composition

Three compositionally and spectrally distinctive Martian dust analogues were selected for this study (see Fig. 1): JSC Mars-1, MGS-1, and MMS-2. The JSC Mars-1 sample is a spectral simulant developed by the Johnson Space Center that mimics the reflectance properties of dust-covered terrains on Mars in visible-near-infrared. It was obtained from the Pu’u Nene cinder cone in Hawaii (Allen et al. 1998), and it displays a brown colour. The H_2O and OH concentrations in the analogue are higher than in Martian dust; however, the removal of volatiles by heating the sample has no significant effect on its scattering properties (Dabrowska et al. 2015).

The Mars Global Simulant (MGS-1) is a mineralogical standard for the Martian basalts, created from the mineralogy produced by the MSL Curiosity rover. It has been developed by extracting individual minerals and has a distinctive grey colour (Cannon et al. 2019).

The Enhanced Mojave Mars Simulant (MMS-2) has been developed by The Martian Garden (<https://www.themartiangarden.com>), which claims it to be the same as the MMS analogue produced by the Jet Propulsion Laboratory because it is mined from the same general

area of the Mojave Desert (Peters et al. 2008). The MMS-2 is red in colour and has added magnesium oxide, iron III oxide, sulphates, and silicates. Detailed sample description and characterization are provided in Martikainen et al. (2024).

2.2 Particle sizes

In this study, we selected two narrow particle size distributions for each simulant: *L* ($7 < d < 40 \mu\text{m}$) and *M* (centred at $d = 3 - 4 \mu\text{m}$), where d is the diameter of a projected surface-area-equivalent sphere. The size fractions were produced by Intituto de Cerámica y Vidrio and further measured with a laser light scattering particle sizer (Malvern Mastersizer 3000). The description of the sample processing and size distribution measurements have been published in Martikainen et al. (2024).

Fig. 2 shows the measured particle size distributions for the *L* and *M* samples. The particle sizer obtains the distribution of surface-equivalent spheres, i.e. the radius of a sphere that has a projected surface area equal to the projected area of the non-spherical particle averaged over all directions. The *L* size fractions have narrow monomodal size distributions. The JSC Mars-1 *M* displays a monomodal distribution; however, the MMS-2 *M* (red squares) has a residual of smaller particles, and the MGS-1 *M* (grey squares) contains a significant amount of small particles creating a bimodal size distribution. In the case of the MGS-1 *M*, scanning electron microscope images show that smaller particles are attached to the surfaces of the *M* particles (see Martikainen et al. 2024). Table 1 lists the effective radii (r_{eff}) and the effective variances (v_{eff}) of the size distributions, as defined by Hansen & Travis (1974).

2.3 Complex refractive indices

The wavelength-dependent complex refractive indices ($m = n + ik$) describe the particle composition: the real part of the complex refractive index, n , describes the ratio of the speed of light in a vacuum to the phase velocity of light in the material, and the

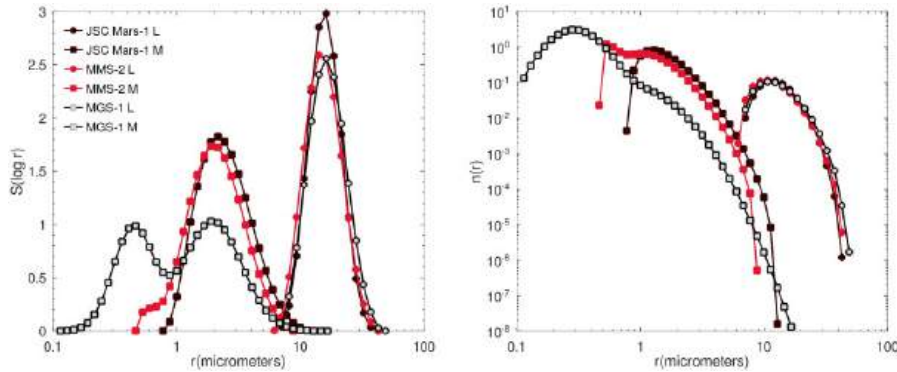


Figure 2. Projected surface area distributions and number distributions of the JSC Mars-1, the MGS-1, and the MMS-2 L and M sizes).

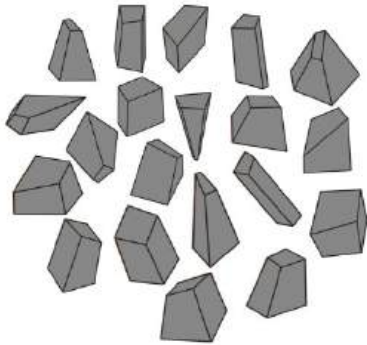


Figure 3. An example of the ensemble irregular hexahedra particles used in the model.

Table 1. The measured effective radii and standard deviations of the samples as shown in Martikainen et al. (2024).

Sample	r_{eff} (μm)	v_{eff}
JSC Mars-1 L	16.5	0.09
JSC Mars-1 M	2.7	0.28
MGS-1 L	17.4	0.12
MGS-1 M	1.6	0.75
MMS-2 L	16.2	0.12
MMS-2 M	2.3	0.28

Table 2. The k -values for the JSC Mars-1, MGS-1, and MMS-2 analogues at 488 and 640 nm retrieved by Martikainen et al. (2024). The n -values were fixed to 1.5.

Sample	$k(488 \text{ nm})$	$k(640 \text{ nm})$
JSC Mars-1	0.00095	0.00065
MGS-1	0.00042	0.00043
MMS-2	0.0011	0.00035

imaginary part, k , describes the absorption of light inside the material. Martikainen et al. (2023) retrieved the complex refractive indices of the three analogues by using advanced numerical techniques together with the measured reflectance spectra and particle size distributions. The imaginary parts for each simulant corresponding to the measurement wavelengths of 488 and 640 nm were provided by Martikainen et al. (2024) and are listed in Table 2.

3 EXPERIMENTAL DATA

The scattering matrix, \mathbf{F} , describes the intensity and the polarization state of the scattered electromagnetic wave. The scattering matrix elements, F_{ij} , depend on the wavelength of the incident light, the direction of the scattering, and the physical properties of the particle. For randomly oriented particles, the scattering direction is defined by the scattering angle ($0 \leq \theta \leq \pi$) which is the angle between the direction of the incoming wave and the direction of the scattered wave. With mirror symmetry, the scattering matrix contains six independent non-zero elements (Hovenier, Mee & Domke 2004):

$$\mathbf{F}(\theta) = \begin{pmatrix} F_{11}(\theta) & F_{12}(\theta) & 0 & 0 \\ F_{12}(\theta) & F_{22}(\theta) & 0 & 0 \\ 0 & 0 & F_{33}(\theta) & F_{34}(\theta) \\ 0 & 0 & -F_{34}(\theta) & F_{44}(\theta) \end{pmatrix}. \quad (1)$$

The scattering matrices of the JSC Mars-1, MGS-1, and MMS-2 L and M size fractions at 488 and 640 nm were measured by Martikainen et al. (2024). The measurements cover scattering angles $\theta = 3^\circ$ to 177° with steps of 1° from $\theta = 1^\circ$ to 10° and from $\theta = 170^\circ$ to 177° , with steps of 5° from $\theta = 10^\circ$ to 155° , and with steps of 2° from $\theta = 155^\circ$ to 170° . For natural incident light, the first element of the scattering matrix, F_{11} , is directly proportional to the scattered flux and is called the phase function. Whereas, the $-F_{12}/F_{11}$ ratio is the degree of linear polarization (DLP). The measurements of these two elements are available for all of the samples as they can be measured using passive remote sensing. The amount of samples set limitations on the measurements, and as such the rest of the non-zero elements were measured for only some size fractions (see Martikainen et al. 2024). The measured scattering matrix \mathbf{F} is proportional to the phase matrix \mathbf{P} by an unknown normalization factor. As the scattering matrix elements near forward and backward scattering angles could not be measured, we use F_{11} and P_{11} -values that are normalized to 1 at a scattering angle of 30° in order to compare laboratory measurements with modelled phase matrices.

4 MODELLING APPROACH

We present a new approach to model Martian dust that uses the full scattering matrices of Martian dust analogues measured in the laboratory for narrow particle size distributions. As the measured dust analogues span over a broad range of particle sizes in both resonance and geometric optics domains at multiple wavelengths, we utilize a single-scattering data base to derive their optical properties.

Initially, two scattering databases that use state-of-the-art numerical techniques were considered: a hexahedra data base (Saito et al.

2021) and a triaxial-ellipsoid data base (Meng et al. 2010). It has been shown that both hexahedra and triaxial ellipsoid models works well in describing scattering by irregular dust particles (Merikallio et al. 2013; Saito et al. 2021) and thus the comparison between the two model particles was of high interest. We do not suggest that the dust grains are hexahedral or triaxial ellipsoids; however, it may be possible to mimic their scattering patterns by using ensembles of these model particles. The tests were carried out using existing experimental data of palagonite, and the results indicated that the hexahedra model was superior to the triaxial ellipsoid model as it could better mimic the scattering pattern of palagonite with fewer free parameters. Furthermore, the range of k values within the triaxial-ellipsoid data base is, in some cases, outside the range needed for the modelling of the JSC Mars-1, MGS-1, and MMS-2 analogues. Therefore, the hexahedra data base was selected to be used for our modelling purposes.

Optical properties of the analogues were acquired from the TAMUdust2020 data base (Saito et al. 2021) that was developed using a combination of three computational methods: the invariant-embedding T-matrix method (Bi et al. 2013), the improved geometric optics method (Yang & Liou 1996), and the physical geometric optics method (Yang & Liou 1997; Yang et al. 2019). The data base consists of pre-calculated single-scattering properties for various ensembles of 20 irregular hexahedral particle models (see Fig. 3) over a broad range of complex refractive indices, particle sizes, particle shapes, and wavelengths. The mixing ratio of each irregular hexahedral particle is determined by the sphericity parameter (Wadell 1935):

$$\Psi_j = \frac{\pi^{1/3}(6V_j)^{2/3}}{A_{S,j}}, \quad (2)$$

where V and A_S are the volume and total surface area of the particle (subscript j is the particle ID). The sphericity parameter defines the amount of particle irregularity within the ensemble so that smaller sphericity indicates a larger amount of particles with high aspect ratios within the ensemble.

In our model, the single-scattering properties obtained from the data base were integrated over the measured particle size distributions. The bulk extinction efficiency $\langle Q_{ext} \rangle$, bulk single-scattering albedo $\langle \omega \rangle$, bulk asymmetry factor $\langle g \rangle$, and bulk phase matrix $\langle \mathbf{P} \rangle$ were computed as (Saito et al. 2021)

$$\langle Q_{ext} \rangle = \frac{\int_{D_{min}}^{D_{max}} n_{SD}(D)A(D, \Psi)Q_{ext}(D, m_r, m_i, \Psi)dD}{\int_{D_{min}}^{D_{max}} n_{SD}(D)A(D, \Psi)dD}, \quad (3)$$

$$\langle \omega \rangle = \frac{\int_{D_{min}}^{D_{max}} n_{SD}(D)A(D, \Psi)Q_{sca}(D, m_r, m_i, \Psi)dD}{\int_{D_{min}}^{D_{max}} n_{SD}(D)A(D, \Psi)Q_{ext}(D, m_r, m_i, \Psi)dD}, \quad (4)$$

$$\langle g \rangle = \frac{\int_{D_{min}}^{D_{max}} n_{SD}(D)A(D, \Psi)Q_{sca}(D, m_r, m_i, \Psi)g(D, m_r, m_i, \Psi)dD}{\int_{D_{min}}^{D_{max}} n_{SD}(D)A(D, \Psi)Q_{sca}(D, m_r, m_i, \Psi)dD}, \quad (5)$$

$$\langle \mathbf{P}(\theta) \rangle = \frac{\int_{D_{min}}^{D_{max}} n_{SD}(D)A(D, \Psi)Q_{sca}(D, m_r, m_i, \Psi)\mathbf{P}(\theta, D, m_r, m_i, \Psi)dD}{\int_{D_{min}}^{D_{max}} n_{SD}(D)A(D, \Psi)Q_{sca}(D, m_r, m_i, \Psi)dD}, \quad (6)$$

where D is the particle diameter, m_r and m_i are the real and imaginary parts of the complex refractive index, Q_{sca} is the scattering efficiency, A is the projected area of the particle, and n_{SD} is the number density. The sum of size-distribution weights, $\sum n_{SD}$, equals unity.

5 RESULTS AND DISCUSSION

We utilize the hexahedra model at 488 and 640 nm together with the measured particle size distributions and derived refractive indices (Sections 2.2 and 2.3) and further compare the model to the measurements. In this section, we review the results and the suitability of the hexahedra model to characterize Martian dust. Finally, we retrieve the single-scattering albedos, extinction efficiencies, extinction cross-sections, and asymmetry factors of the analogues for a wavelength range of 200–2000 nm using the hexahedra model.

5.1 Sphericity

As discussed in Section 4, the sphericity parameter plays an important role in defining the axis ratios within the ensemble of hexahedra model particles, making it a key parameter to study. Validation of the sphericity parameter for the irregular hexahedra model against geometric shapes confirmed that lower sphericity values correspond well to the observed geometries of dust particles (Saito & Yang 2021). To comprehensively explore the range of the sphericity parameter, values from 0.695 (minimum) to 0.785 (maximum) were employed in this study.

In Figs 4 and 5, we show the effect of different sphericity values on the modelled scattering matrices of the MGS-1 L and M samples at 640 nm. In the case of the L sample, the highest value produces a significant overestimation in the side- and back-scattering directions of the phase function, and a peak in the DLP curve at around 30° that does not exist in the measurements. For the M sample, high sphericity generates large discrepancies between the measured and modelled DLP curves and an increasing phase curve towards the backscattering direction. Furthermore, high sphericity values create larger differences in all of the other scattering matrix elements. For our study, we choose a sphericity of 0.71 as it produces the best fits overall and is within the recommended values.

5.2 Wavelength and composition

Mie theory has been widely used for homogeneous spherical particles to interpret photometric and polarimetric behaviour of dust due to its simplicity over more complex models. The light-scattering computations for spheres can be carried out with efficiency for a broad range of complex refractive indices and sizes. However, it is well known that using spherical shapes to characterize irregular dust particles can produce large errors in the retrieved optical properties (see e.g. Mishchenko et al. 2003; Dubovik et al. 2006; Muñoz et al. 2021). In this section, we compare the measured scattering matrices of the three analogues to the computations carried out using the hexahedra model and a model that uses spheres.

5.2.1 L size fraction

The measured and modelled scattering matrices of the JSC Mars-1, MGS-1, and MMS-2 L samples at 488 and 640 nm are shown in Figs 6–8. The results indicate that the measured scattering matrices of irregular dust particles cannot be accurately modelled with spheres, whereas the hexahedra model is able to mimic the scattering pattern reasonably well. Consequently, we focus on analysing the computed scattering matrices that were retrieved using the hexahedra model. In the case of all of the analogues, the L size fraction is more difficult to reproduce than the M size fraction. The hexahedra model underestimates the phase function at side- and backscattering directions, and the modelled $P_{34}(\theta)/P_{11}(\theta)$ and $P_{44}(\theta)/P_{11}(\theta)$ elements

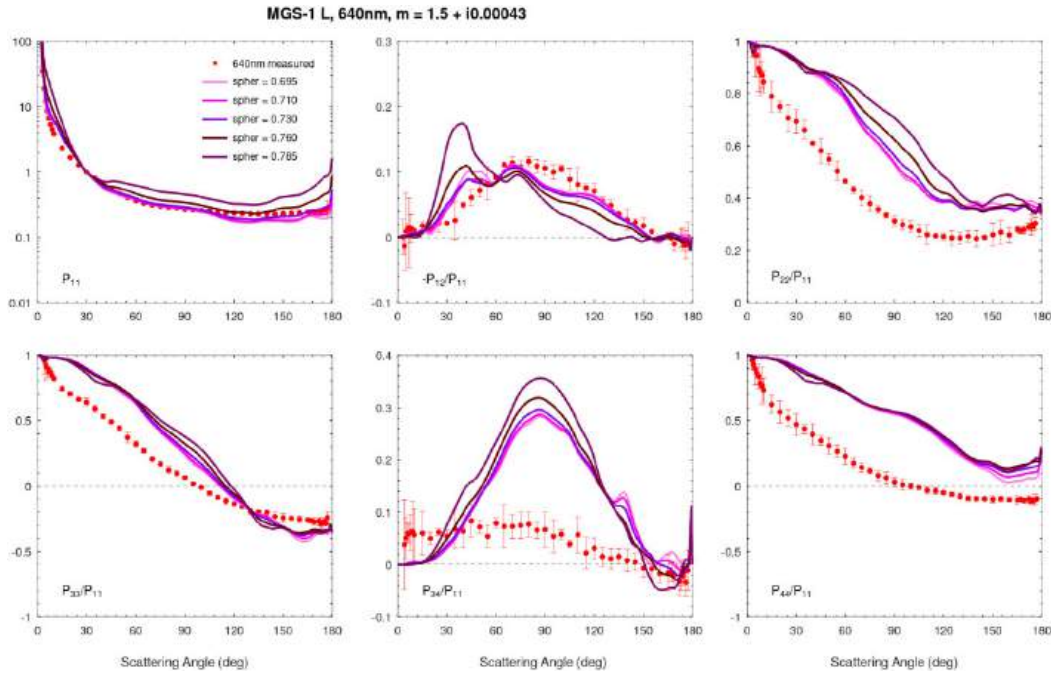


Figure 4. The measured and modelled scattering matrices of the MGS-1 L sample at 640 nm using different sphericity values.

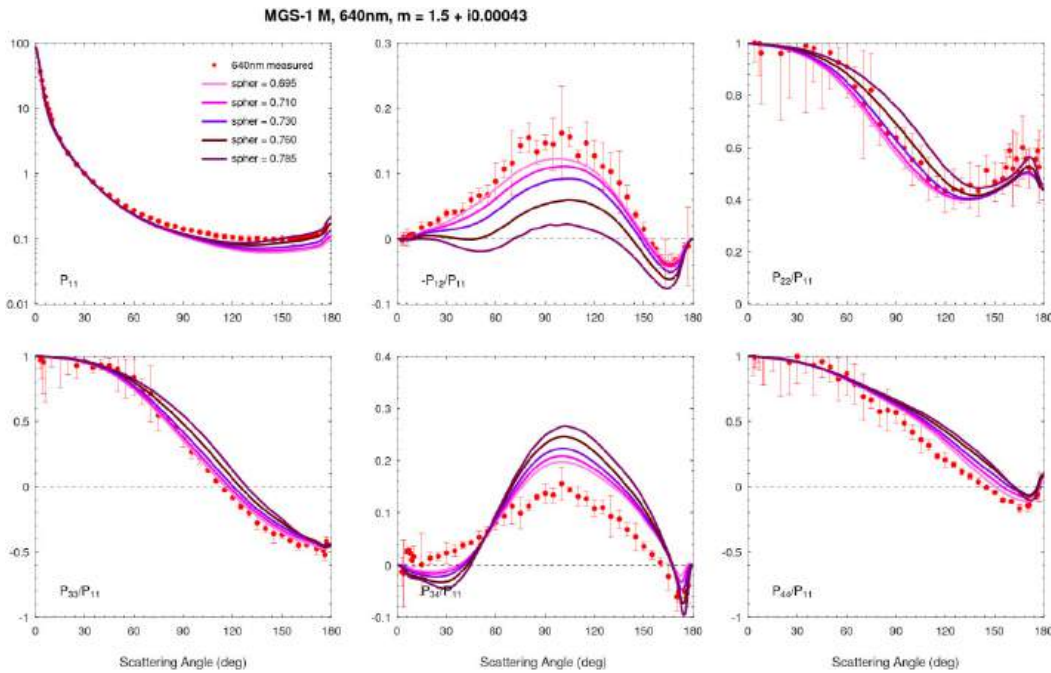


Figure 5. The measured and modelled scattering matrices of the MGS-1 M sample at 640 nm using different sphericity values.

are much larger than the measured ones. The DLP curves can be modelled well for the MGS-1 analogue, however, the modelled maximum DLP of the JSC Mars-1 and MMS-2 analogues at 488 nm is underestimated and slightly shifted to smaller scattering angles. The features of the measured $P_{22}(\theta)/P_{11}(\theta)$ -curves cannot be mimicked well with the model as there are differences in both absolute values and shapes of the curves. The modelled $P_{33}(\theta)/P_{11}(\theta)$ -element of the JSC Mars-1 analogue shows a good fit to the measurements in blue and red, whereas for the MGS-1 and MMS-2 analogues the differences are larger. The discrepancies between

the measurements and the model become larger with increasing absorption.

The model assumes hexahedra particles with smooth surfaces and no internal structure. In contrast, natural irregular dust particles contain wavelength-scale surface structure and internal inhomogeneities, which enhance multiple scattering within a single particle. Here, multiple scattering specifically refers to electromagnetic interactions with the boundaries and inhomogeneities of a single particle, distinguishing it from scattering interactions occurring among separate particles. The effect of multiple scattering becomes

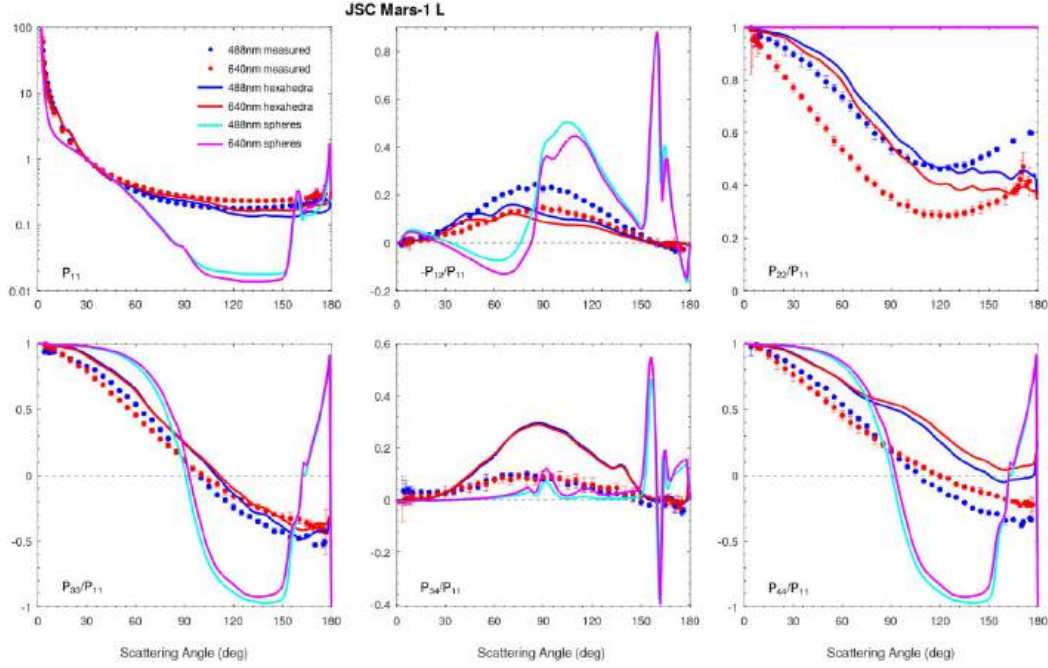


Figure 6. The measured scattering matrices of the JSC Mars-1 L sample at 488 and 640 nm compared to the hexahedra model and a model that uses spheres.

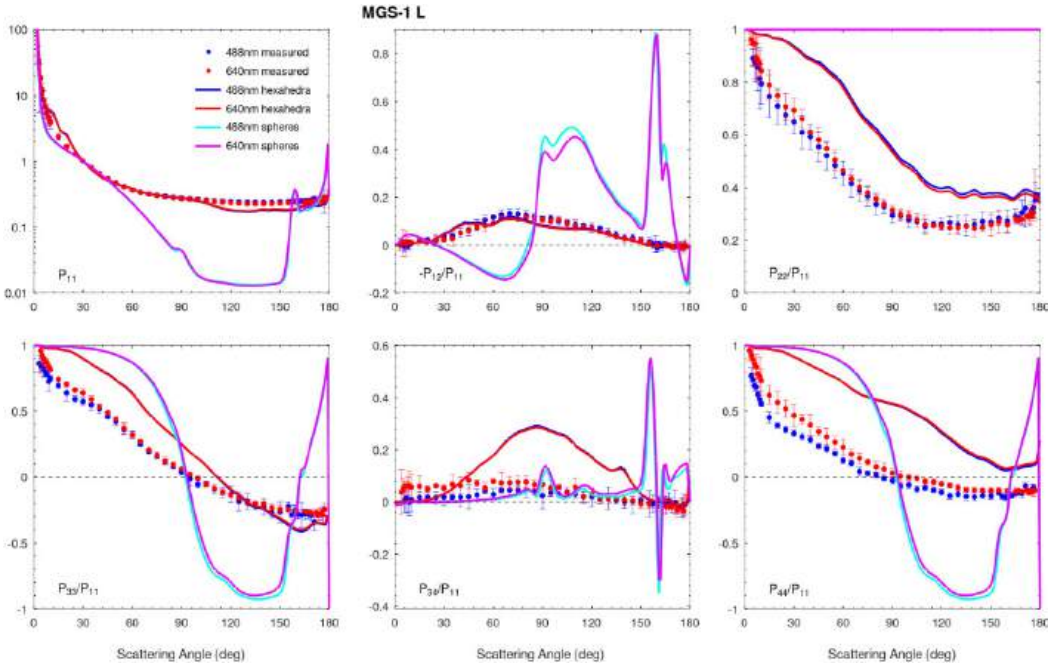


Figure 7. The measured scattering matrices of the MGS-1 L sample at 488 and 640 nm compared to the hexahedra model and a model that uses spheres.

more pronounced as particle size increases, since larger particles have more complex external and internal structures. Escobar-Cerezo et al. (2017) showed that by adding internal inclusions and wavelength-scale structure to the particle the phase curve flattens and increases at side- and backscattering directions, the $P_{22}(\theta)/P_{11}(\theta)$ element decreases and produces a steeper slope towards backscattering direction, the $P_{33}(\theta)/P_{11}(\theta)$ and $P_{44}(\theta)/P_{11}(\theta)$ elements decrease, and the $P_{34}(\theta)/P_{11}(\theta)$ element flattens significantly. We also note that the measured negative polarization branch (NPB) of the L analogues cannot be modelled using smooth hexahedra particles as it is assumed

to be caused by wavelength-scale surface structure and/or internal inclusions (see Martikainen et al. 2024).

5.2.2 *M* size fraction

In Figs 9–11, we show the measured and modelled scattering matrices of the JSC Mars-1, MGS-1, and MMS-2 M samples at 488 and 640 nm. Due to the limited amount of sample M, we could not perform measurements for all scattering matrix elements at 488 nm.

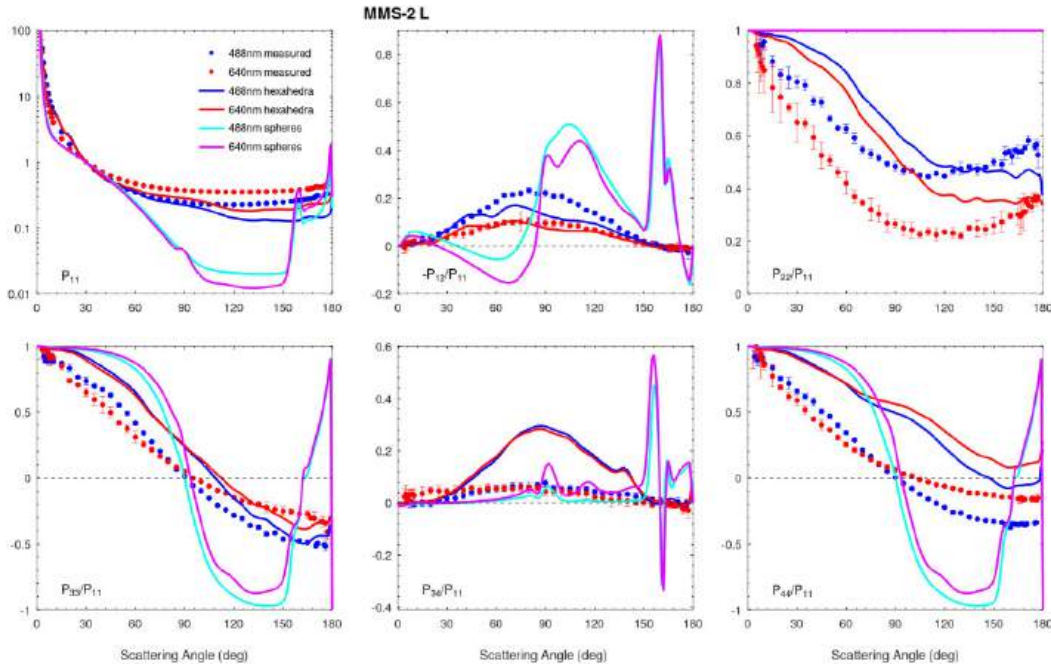


Figure 8. The measured scattering matrices of the MMS-2 L sample at 488 and 640 nm compared to the hexahedra model and a model that uses spheres.

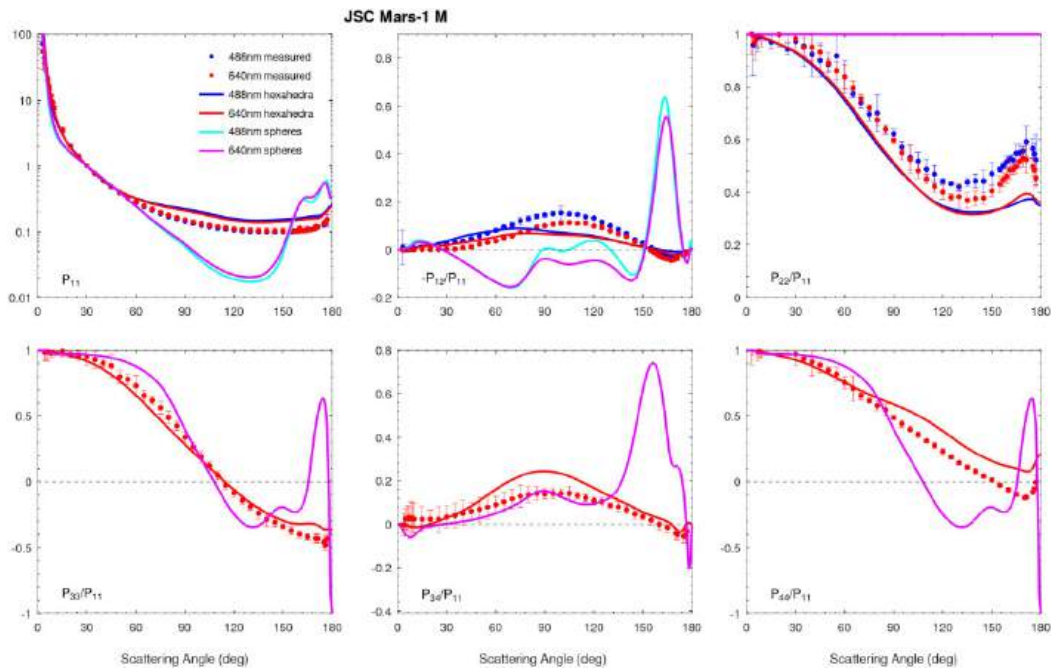


Figure 9. The measured scattering matrices of the JSC Mars-1 M sample at 488 and 640 nm compared to the hexahedra model and a model that uses spheres.

Similarly to the L size fraction, a model that uses spheres is not able to reproduce well any of the measured scattering matrices of the M size fraction, and thus our focus is on the hexahedra model. Generally, the modelled scattering matrix elements of the MGS-1 analogue produce the best fits to the measurements; however, the model slightly underestimates the phase function at side- and backscattering directions at both wavelengths. The DLP curve can be modelled reasonably well with a distinguishable NPB, although the measured maxima of the DLP curves are somewhat larger than the modelled values. The modelled $P_{22}(\theta)/P_{11}(\theta)$, $P_{33}(\theta)/P_{11}(\theta)$,

and $P_{44}(\theta)/P_{11}(\theta)$ elements mimic the measurements well, whereas the modelled $P_{34}(\theta)/P_{11}(\theta)$ element shows small differences when compared to the measurements. In overall, the model can reproduce the MGS-1 measurements well in blue and red.

The modelled JSC Mars-1 and MMS-2 M samples show a similar behaviour: the modelled phase functions are slightly overestimated at side- and backscattering directions, and the modelled maxima of the DLP curves are underestimated. In the case of the JSC Mars-1 analogue, the maxima of the DLP are shifted towards smaller scattering angles at both wavelengths, whereas the MMS-2 sample

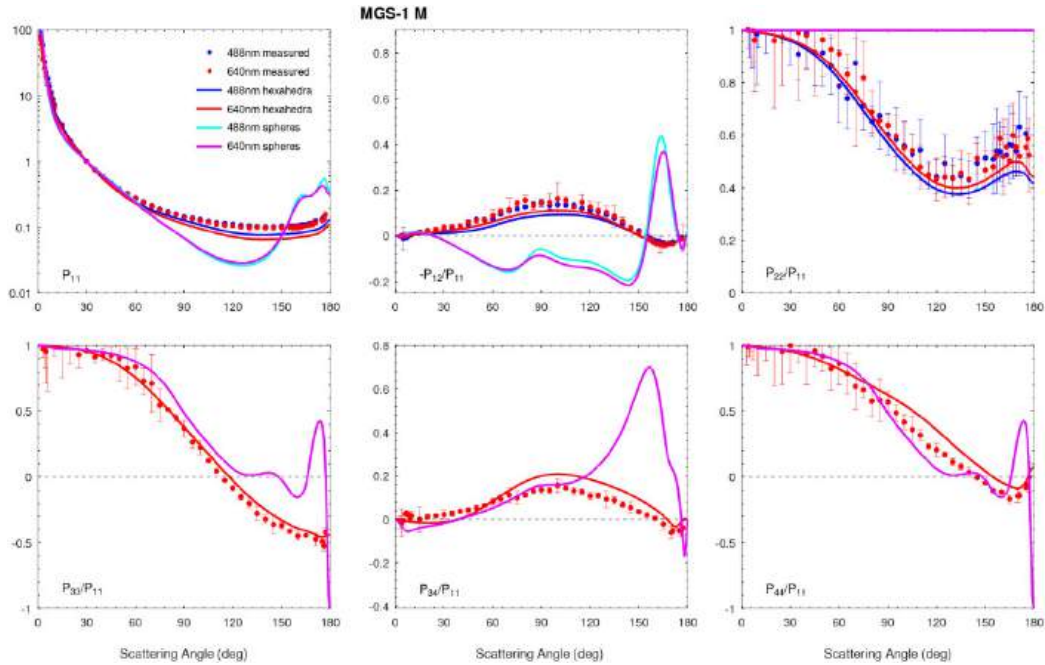


Figure 10. The measured scattering matrices of the MGS-1 M sample at 488 and 640 nm compared to the hexahedra model and a model that uses spheres.

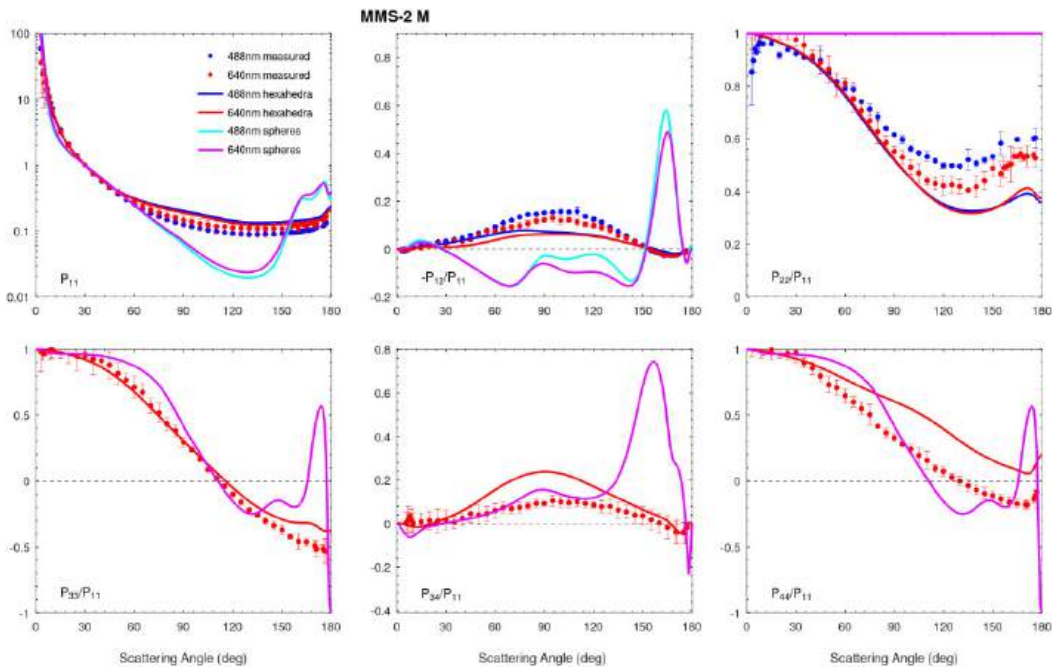


Figure 11. The measured scattering matrices of the MMS-2 M sample at 488 and 640 nm compared to the hexahedra model and a model that uses spheres.

shows a similar shift only in blue. Furthermore, the modelled NPB for the JSC Mars-1 analogue is shallower at both wavelengths. The modelled $P_{22}(\theta)/P_{11}(\theta)$ element underestimates the backscattering direction to some extent for both analogues, whereas the $P_{33}(\theta)/P_{11}(\theta)$ elements can be modelled well. Similarly to MGS-1, the modelled $P_{34}(\theta)/P_{11}(\theta)$ element shows some differences to the measured values for the two analogues. Finally, the $P_{44}(\theta)/P_{11}(\theta)$ element becomes overestimated at side- and backscattering angles.

It should be emphasized that the angular distribution of the phase function is important for estimating particle size distributions

(PSDs), as the forward scattering produced by diffraction carries significant information about PSDs. Normalizing the phase function at a scattering angle of 30° due to the unavailability of exact forward scattering intensity introduces several uncertainties in PSD estimates that rely solely on the P_{11} -element of the scattering matrix. Key sources of uncertainty include the loss of absolute intensity information, which is important for accurate size determination, and the exclusion of forward scattering data, which is particularly sensitive to larger particle sizes. Additionally, normalizing at a specific angle may distort the angular scattering distribution, es-

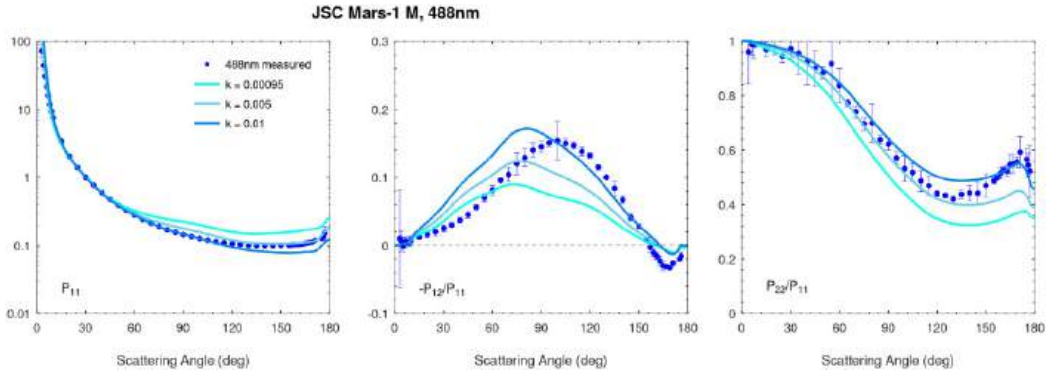


Figure 12. The measured and modelled scattering matrices of the JCS Mars-1 M sample at 488 nm using different k values.

pecially for irregular particles, and amplify measurement noise or errors at the normalization angle. PSD estimates also become more reliant on theoretical models, increasing sensitivity to assumptions about particle properties such as refractive index and shape. These challenges underscore the importance of studying the full scattering matrix for a more comprehensive understanding.

Given that our model is highly sensitive to the particle size distribution and the complex refractive index (both n and k), sensitivity tests have been conducted in Section 5.3 to investigate their impact on the modelled scattering matrices.

5.3 A sensitivity study

In this section, we carry out sensitivity tests to study the effect of absorption, real part of the complex refractive index, and particle size distribution within the hexahedra model in order to understand their contribution to the modelled scattering matrix elements. The sensitivity study was performed on all of the analogues; however, here we present the results for the JCS Mars-1 as a case study.

5.3.1 Absorption

The k values of the analogues were previously retrieved by Martikainen et al. (2023) from their measured reflectance spectra, however, it is of interest to study how changing the k affects the modelled scattering matrices of the M and L size fractions. For this test, we utilize a range of k values from 0.00095 to 0.01 at 488 nm that showed the largest differences between the measured and modelled DLP curves when using the retrieved values of Martikainen et al. (2024).

In Fig. 12, we present the modelled scattering matrix elements of the JCS Mars-1 M size using different k values. The results show that increasing absorption decreases the phase function at the backscattering direction, increases the maximum of the DLP curve, and shifts the inversion angle towards larger scattering angles. The $P_{22}(\theta)/P_{11}(\theta)$ element shows an increase at side- and backscattering angles. In overall, increasing absorption in the model for the M sample seems to fit the measurements better. However, the shift of the inversion angle deviates the model further from the measured NPB, and the shift in the location of the maximum DLP cannot be explained by increasing absorption.

It is important to repeat the test using the L sample since absorption plays a major role in larger particles. As the material stays the same, with changing only the particle size distribution, the same complex refractive index should be used for both L and M samples. In Fig. 13, we have carried out the test for the JCS Mars-1 L size. Now,

changes in absorption cause enormous differences as the model blows out of proportion: the phase curve becomes heavily underestimated at side- and backscattering directions, the maximum of the DLP curve is greatly overestimated, and the $P_{22}(\theta)/P_{11}(\theta)$, $P_{33}(\theta)/P_{11}(\theta)$, and $P_{44}(\theta)/P_{11}(\theta)$ elements show large discrepancies between the measured and modelled values. Furthermore, incorporating the internal and/or external structure, as proposed in Section 5.2.1, would not sufficiently address the significant discrepancies observed in the phase function, DLP curve, and the $P_{22}(\theta)/P_{11}(\theta)$ element. Additionally, it would exacerbate the differences in the $P_{33}(\theta)/P_{11}(\theta)$, $P_{34}(\theta)/P_{11}(\theta)$, and $P_{44}(\theta)/P_{11}(\theta)$ elements.

In the case of the three analogues, increasing absorption is not a viable option. The k values retrieved by Martikainen et al. (2023) produce the best fits in general for both the spectral data and the measured scattering matrices, and should thus be used when retrieving optical properties for the analogues. We note that optical constants of Martian dust aerosols that have been retrieved from observations using small particle sizes and simplified particle shapes should be used with caution for larger particles in the geometric optics domain as they tend to produce too much absorption (see e.g. Martikainen et al. 2023). Mishchenko et al. (1997) showed that increasing absorption decreases the differences in the phase function between irregular dust and spherical particles; however, Muñoz et al. (2021) concluded that while unrealistically high absorption produces a better fit to the measured phase function it also generates large errors in the degree of linear polarization. In addition, unrealistically high absorption values have a strong effect on the single-scattering albedo.

Our results reinforce the significance of considering polarization, as relying solely on the phase function fails to provide a comprehensive understanding of the material optical properties. This is particularly critical when employing a model that incorporates a simplified particle shape and multiple free parameters, such as particle size and complex refractive index. Moreno et al. (2002) and Stam & Hovenier (2005) demonstrated that disregarding the polarized nature of light results in substantial errors in determining the scattered contribution to the measured flux. It introduces wavelength-dependent inaccuracies in atmospheric optical thickness, which, in turn, affect the gaseous mixing ratios (i.e. abundances) derived from these spectra (Stam & Hovenier 2005).

5.3.2 Real part of the refractive index

The imaginary parts of the complex refractive indices were previously derived by Martikainen et al. (2023) (Table 2) from the measured reflectance spectra. Their sensitivity analysis indicated

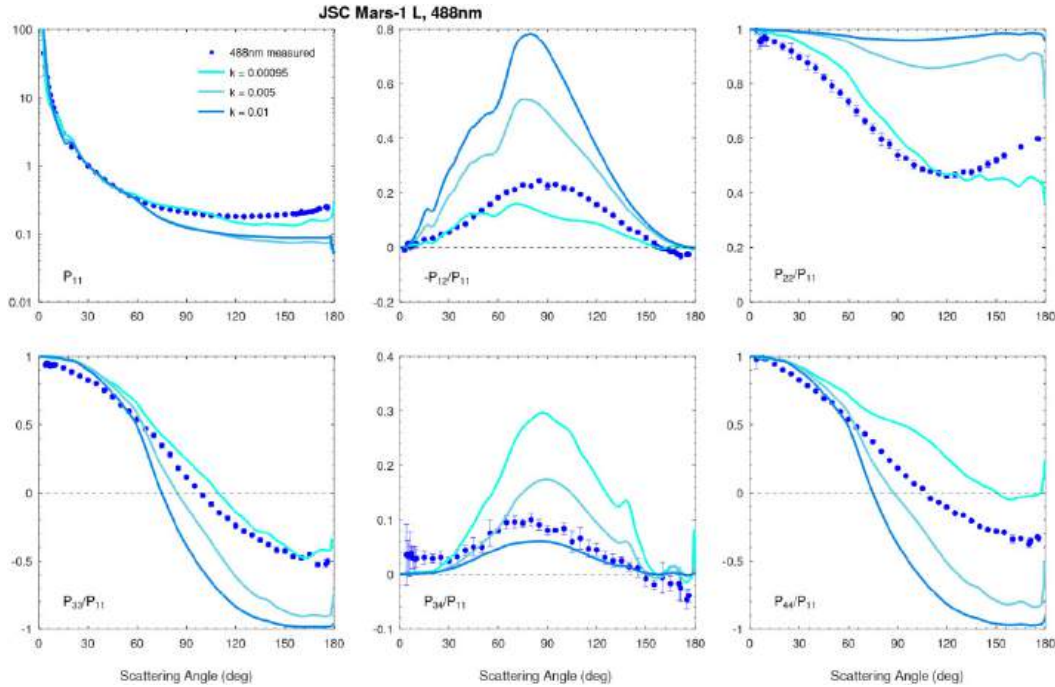


Figure 13. The measured and modelled scattering matrices of the JCS Mars-1 L sample at 488 nm using different k values.

that the derived values were not significantly affected by variations in n -values within the range of 1.4–1.6. However, scattering matrix elements are known to exhibit sensitivity to the real part of the complex refractive index (see e.g. Huang et al. 2020; Saito et al. 2021). Therefore, examining the influence of n on the measured scattering matrix elements can provide deeper insights into the scattering behaviour of irregular dust particles.

Here, we perform a sensitivity study by varying the real part of the complex refractive index for the JCS Mars-1 analogue. Similarly to Martikainen et al. (2023), we selected the range of 1.4 – 1.6 that is typically used for silicates. We utilize the M size fraction as the effects caused by wavelength-scale surface roughness and/or internal structure are less prominent than for the L size fraction.

In Figs 14 and 15, we show the measured and modelled scattering matrices of the JCS Mars-1 M sample at 488 and 640 nm with different n -values. At both wavelengths, increasing n flattens the phase function at side- and backscattering angles, shifts the location of the maximum DLP and the inversion angle towards smaller scattering angles, and slightly decreases the maximum of the NPB. At 488 nm, the maximum DLP values increase with larger n , while the opposite is true at 640 nm. The $P_{22}(\theta)/P_{11}(\theta)$, $P_{33}(\theta)/P_{11}(\theta)$, and $P_{34}(\theta)/P_{11}(\theta)$ elements exhibit small differences with changing n , whereas the $P_{44}(\theta)/P_{11}(\theta)$ curve increases noticeably with increasing n .

5.3.3 Size distribution

The sensitivity tests performed in Sections 5.3.1 and 5.3.2 confirmed that the measured DLP curves, especially the NPB of the JCS Mars-1 M sample, cannot be explained with the hexahedra model by changing the real and imaginary parts of the complex refractive index, thus, looking at the SEM images and the measured particle size distribution can provide more insight. When measuring particle size distributions that contain particles smaller than 1 μm , the measurement uncertainties become larger as the small particles

tend to stick to the surfaces of the larger grains. The measured size distributions of the MGS-1 and MMS-2 M samples show a presence of small particles that can be further confirmed by the SEM images, however, the measured M size fraction of the JCS Mars-1 analogue exhibits a clean monomodal distribution. Examining the SEM image of the JCS Mars-1 M sample (Fig. 1) suggests that there is a population of small particles that cannot be seen in its measured particle size distribution. Therefore, we carried out a sensitivity test by increasing the amount of small particles and decreasing the amount of large particles to account for the effect of particle aggregation during the size distribution measurements and their eventual separation during the scattering matrix measurements. The particle size distribution used in the test is shown in Fig. 16 together with the original size distribution of the JCS Mars-1 M sample.

Fig. 17 shows the modelled scattering matrices of the JCS Mars-1 M sample using the particle size distributions shown in Fig. 16. At both wavelengths, we used the imaginary part of the complex refractive index for JCS Mars-1 listed in Table 2. At 488 nm, the particle size distribution with added small particles produces the best fit by using $n = 1.45$, whereas at 640 nm, the best fit was obtained with $n = 1.5$. The original size distribution was used with $n = 1.5$ in both blue and red. The results show that adding small particles decreases the phase function at side and backscattering directions, increases the NPB, shifts the location of the maximum DLP toward larger wavelengths, and decreases the inversion angle. In general, the model reproduces the measurements better with the new size distribution indicating that in the case of the JCS Mars-1 M sample the measured particle size distribution does not account for the small particle population seen in the SEM image.

Although small differences exist between the measured and modelled scattering matrices, sensitivity tests have demonstrated that the hexahedra model achieves a level of accuracy in reproducing the measurements that a simpler spherical model cannot attain. Of particular interest are the huge discrepancies at side- and back-

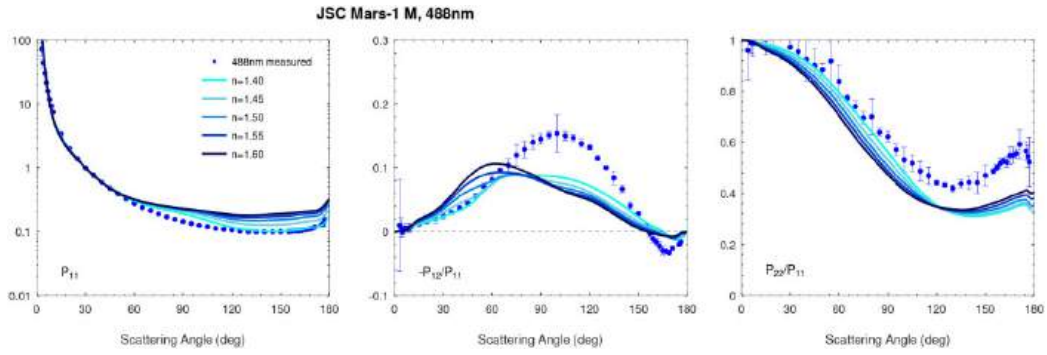


Figure 14. The measured and modelled scattering matrices of the JCS Mars-1 M sample at 488 nm using different n -values.

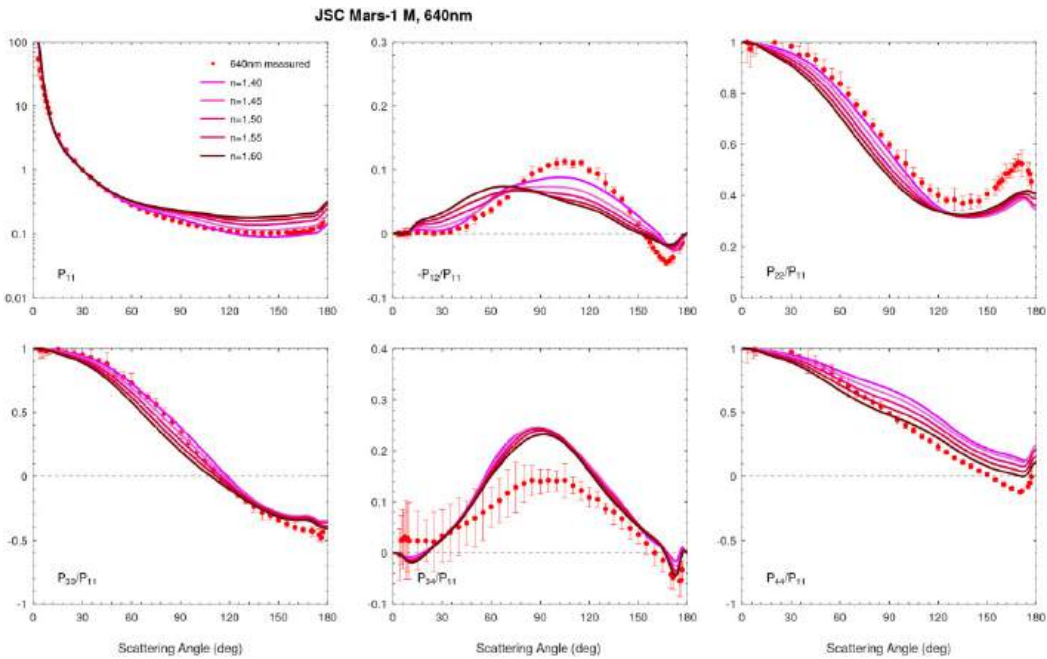


Figure 15. The measured and modelled scattering matrices of the JCS Mars-1 M sample at 640 nm using different n -values.

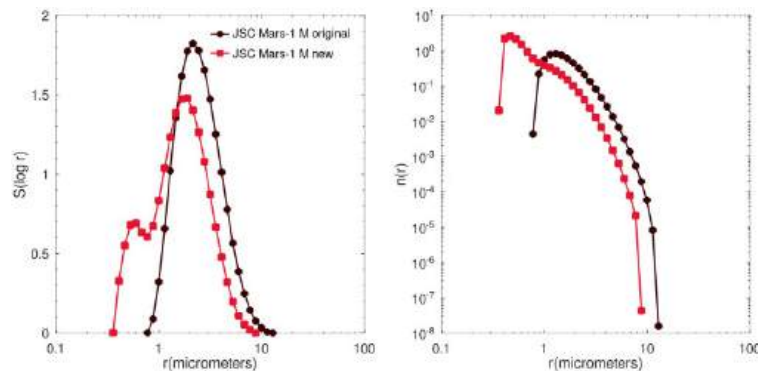


Figure 16. Projected surface area distributions and number distributions of the original JCS Mars-1 M size and the new particle size distribution with added small particles.

scattering regions between the experimental phase functions and those calculated using spheres. Previous studies that focus on retrieving optical properties of Martian aerosols from observations (e.g. Tomasko et al. 1999; Markiewicz et al. 2002; Wolff et al. 2009) do not account for the full scattering matrix and thus a large part of

information on the particle shape, size, and complex refractive index is lost. Having access to the measured particle sizes, SEM images, diffuse reflectance spectra, and the full scattering matrices provides us with tools to fully understand the scattering behaviour of irregular dust grains and to validate the used particle models.

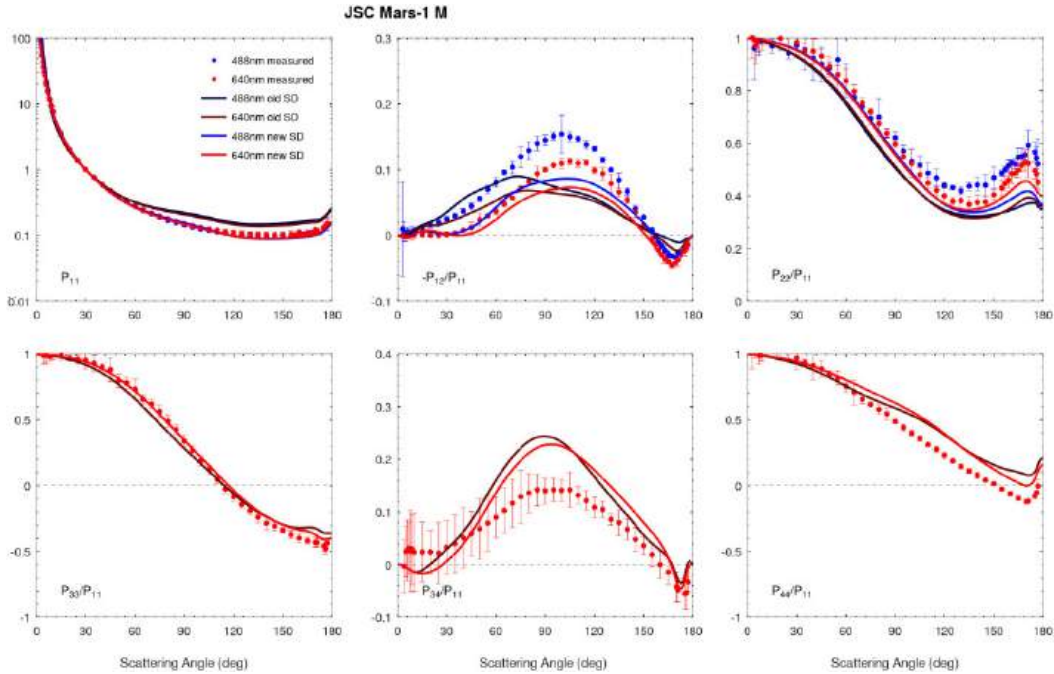


Figure 17. The measured and modelled scattering matrices of the JCS Mars-1 M sample at 488 and 640 nm using the particle size distributions shown in Fig. 16.

5.4 Retrieval of optical properties

Optical properties of Martian dust aerosols are needed in radiative-transfer models to account for multiple scattering by dust in the atmosphere and thus to better understand the global climate. Here, we utilize the hexahedra model to retrieve bulk extinction efficiencies $\langle Q_{\text{ext}} \rangle$, single-scattering albedos $\langle \omega \rangle$, asymmetry factors $\langle g \rangle$, extinction cross-sections $\langle \sigma_{\text{ext}} \rangle$, and phase matrices $\langle \mathbf{P} \rangle$ for the JCS Mars-1, MGS-1, and MMS-2 analogues. The retrieval was carried out for the wavelength range of 200–2000 nm using the k -values retrieved by Martikainen et al. (2023) and the best-fitting parameters from the sensitivity study performed in Section 5.3. For JCS Mars-1, we used $n = 1.45$ from 200 to 500 nm, $n = 1.50$ from 550 to 2000 nm, and the particle size distribution with added amount of small particles that was introduced in Section 5.3.3. For MGS-1 and MMS-2, we used $n = 1.50$ throughout the entire wavelength range, and the measured size distributions shown in Fig. 2. The retrieved $\langle Q_{\text{ext}} \rangle$, $\langle \omega \rangle$, $\langle g \rangle$, and $\langle \sigma_{\text{ext}} \rangle$ for the L sizes are listed in Appendix A, Table A1, and the for the M sizes in Table A2. The $\langle \mathbf{P} \rangle$ for each wavelength are available at the Granada-Amsterdam light-scattering data base.

6 CONCLUSIONS

We have studied the suitability of a hexahedra model to mimic light scattering by the JCS Mars-1, MGS-1, and MMS-2 Martian dust analogues with L and M narrow particle size distributions by comparing the simulations against the corresponding scattering matrices measured in laboratory at 488 and 640 nm. First, we investigated how well the scattering matrix elements could be reproduced by using hexahedra shapes with different aspect ratios, and further compared them to a model that uses spheres. Then, we performed sensitivity studies to understand how different assumptions of the complex refractive index and particle size distribution affect the modelled optical properties.

Our results indicate that the hexahedra model performs well in reproducing the M size distribution; however, the discrepancies between the measured and modelled scattering matrices become more pronounced as particle size increases. This may be attributed to wavelength-scale surface roughness and internal inhomogeneities that induce multiple scattering within individual large dust grains that is not accounted for by the smooth hexahedra model particles. Overall, the hexahedra model provides a significantly better fit to the scattering matrix elements compared to a model using spheres.

The sensitivity studies let us fine tune the complex refractive indices and examine the measured particle size distributions in detail. Increasing the real part of the complex refractive index flattens the phase function at side- and backscattering angles, shifts the location of the maximum DLP and the inversion angle toward smaller scattering angles, and slightly decreases the maximum of the NPB. Furthermore, increasing the imaginary part of the complex refractive index decreases the phase function at the backscattering direction, increases the maximum of the DLP curve, and shifts the inversion angle to larger scattering angles. Additionally, the $P_{22}(\theta)/P_{11}(\theta)$ element shows a substantial increase at side- and backscattering angles. The k values retrieved by Martikainen et al. (2023) provide the best overall fits for both the spectral data and the measured scattering matrices, making them the preferred choice for retrieving optical properties of the analogues. Increasing k is not a viable option, as absorption significantly impacts the L size distribution and blows the modelled scattering matrix elements out of proportion with a slight increase. The NPB and the shift in the location of the maximum DLP for the JCS Mars-1 M sample cannot be fully explained by changing either the real or imaginary part of the complex refractive index. Examination of the SEM image reveals a population of small particles that are not captured in the measured particle size distribution. To address this discrepancy, we conduct a sensitivity test by increasing the proportion of small particles and reducing the proportion of large particles to account for particle aggregation during size distribution measurements and their subsequent separation during scattering

matrix measurements. The model reproduces the measurements better when using the adjusted size distribution, suggesting that the measured particle size distribution for the JSC Mars-1 M sample does not accurately reflect the small particle population observed in the SEM image.

Finally, by using the best-fitting parameters from the sensitivity studies, we retrieve bulk extinction efficiencies, single-scattering albedos, asymmetry factors, extinction cross-sections, and phase matrices for the L and M size distributions of the JSC Mars-1, MGS-1, and MMS-2 analogues from 200 to 2000 nm, capturing a broad range of spectral variability. These values provide a foundation for radiative-transfer simulations aimed at improving our understanding of Martian atmospheric dust. This study highlights the importance of incorporating the full scattering matrix in optical property retrievals, as significant information about particle shape, size, and complex refractive index is lost when polarization is omitted.

ACKNOWLEDGEMENTS

This work was supported by the European Union's Horizon 2020 research and innovation program (grant agreement no. 101004052). Research by JM, OM, JCGM, and MP has been partially supported by PID2021-123370OB-100/AEI/10.13039/501100011033/FEDER and Severo Ochoa grant CEX2021-001131-S funded by MCIN/AEI/10.13039/501100011033.

DATA AVAILABILITY

The retrieved optical properties are freely available at the Granada–Amsterdam light-scattering data base (scattering.iaa.es) under the Martian analogue category (JSC Mars-1 L, JSC Mars-1 M, MGS-1 L, MGS-1 M, MMS-2 L, and MMS-2 M). We kindly request that you cite both this paper and Muñoz et al. (2025) when using the data.

REFERENCES

- Allen C. C., Morris R. V., Jager K. M., Golden D. C., Lindstrom D. J., Lindstrom M. M., Lockwood J. P., 1998, in *Lunar and Planetary Science Conference, Texas, Lunar and Planetary Institute*. p. 1690
- Bi L., Yang P., Kattawar G. W., Mishchenko M. I., 2013, *J. Quant. Spectrosc. Radiat. Transfer*, 116, 169
- Cannon K. M., Britt D. T., Smith T. M., Fritsche R. F., Batchelder D., 2019, *Icarus*, 317, 470
- Dabrowska D. D., Muñoz O., Moreno F., Ramos J. L., Martínez-Frías J., Wurm G., 2015, *Icarus*, 250, 83
- Dubovik O. et al., 2006, *J. Geophys. Res. Atmos.*, 111, D11
- Escobar-Cerezo J., Palmer C., noz O. M., Moreno F., Penttilä A., Muinonen K., 2017, *ApJ*, 838, 74
- Hansen J. E., Travis L. D., 1974, *Space Sci. Rev.*, 16, 527
- Hovenier J. W., Mee C., Domke H., 2004, *Transfer of polarized light in planetary atmospheres*. Springer, Dordrecht, p. 1
- Huang Y., Liu C., Yao B., Yin Y., Bi L., 2020, *Atmos. Chem. Phys.*, 20, 2865
- Markiewicz W., Keller H., Thomas N., Titov D., Forget F., 2002, *Adv. Space Res.*, 29, 175
- Martikainen J. et al., 2023, *ApJS*, 268, 47
- Martikainen J. et al., 2024, *ApJS*, 273, 28
- Meng Z., Yang P., Kattawar G. W., Bi L., Liou K., Laszlo I., 2010, *J. Aerosol Sci.*, 41, 501
- Merikallio S., Nousiainen T., Kahnert M., Harri A.-M., 2013, *Opt. Express*, 21, 17972
- Mishchenko M. I., Travis L. D., Kahn R. A., West R. A., 1997, *J. Geophys. Res.*, 102, 16831
- Mishchenko M. I. et al., 2003, *J. Quant. Spectrosc. Radiat. Transfer*, 79–80, 953
- Moreno F., Muñoz O., López-Moreno J. J., Molina A., Ortiz J. L., 2002, *Icarus*, 156, 474
- Muñoz O. et al., 2021, *ApJS*, 256, 17
- noz O. M. et al., 2025, *J. Quant. Spectrosc. Radiat. Transfer*, 331, 109252
- Peters G. H., Abbey W., Bearman G. H., Mungas G. S., Smith J. A., Anderson R. C., Douglas S., Beegle L. W., 2008, *Icarus*, 197, 470
- Saito M., Yang P., 2021, *Geophys. Res. Lett.*, 48, e2021GL095121
- Saito M., Yang P., Ding J., Liu X., 2021, *J. Atmos. Sci.*, 78, 2089
- Stam D. M., Hovenier J. W., 2005, *A&A*, 444, 275
- Tomasko M. G., Doose L. R., Lemmon M., Smith P. H., Wegryn E., 1999, *J. Geophys. Res. Planets*, 104, 8987
- Wadell H., 1935, *J. Geol.*, 43, 250
- Wolff M. J. et al., 2006, *J. Geophys. Res. Planets*, 111, E12S17
- Wolff M. J., Smith M. D., Clancy R. T., Arvidson R., Kahre M., Seelos IV F., Murchie S., Savijärvi H., 2009, *J. Geophys. Res. Planets*, 114, E00D04
- Wolff M. J., Todd Clancy R., Goguen J. D., Malin M. C., Cantor B. A., 2010, *Icarus*, 208, 143
- Yang P., Ding J., Panetta R. L., Liou K.-N., Kattawar G., Mishchenko M. I., 2019, *Progr. Electromagn. Res.*, 164, 27
- Yang P., Liou K. N., 1996, *Appl. Opt.*, 35, 6568
- Yang P., Liou K.-N., 1997, *J. Optical Soc. Am. A-Opt. Image Sci. Vis.*, 14, 2278

APPENDIX A: OPTICAL PROPERTIES

Table A1. Optical properties retrieved for the JSC Mars-1, MGS-1, and MMS-2 L size fractions using the hexahedra model.

λ (nm)	JSC Mars-1 L				MGS-1 L				MMS-2 L			
	$\langle Q_{ext} \rangle$	$\langle \omega \rangle$	$\langle g \rangle$	$\langle \sigma_{ext} \rangle$	$\langle Q_{ext} \rangle$	$\langle \omega \rangle$	$\langle g \rangle$	$\langle \sigma_{ext} \rangle$	$\langle Q_{ext} \rangle$	$\langle \omega \rangle$	$\langle g \rangle$	$\langle \sigma_{ext} \rangle$
200	2.0149	0.6279	0.9218	1184.10	2.0125	0.7424	0.8464	1224.00	2.0128	0.7019	0.8716	1061.32
225	2.0161	0.6260	0.9226	1184.79	2.0136	0.7345	0.8513	1224.64	2.0139	0.6993	0.8729	1061.90
250	2.0173	0.6363	0.9171	1185.53	2.0145	0.7425	0.8462	1225.23	2.0150	0.7008	0.8721	1062.49
275	2.0183	0.6391	0.9155	1186.13	2.0156	0.7606	0.8351	1225.87	2.0161	0.7090	0.8669	1063.07
300	2.0197	0.6544	0.9069	1186.91	2.0166	0.7828	0.8213	1226.47	2.0172	0.7196	0.8602	1063.62
325	2.0208	0.6638	0.9015	1187.55	2.0175	0.8022	0.8095	1227.01	2.0182	0.7306	0.8533	1064.14
350	2.0223	0.6868	0.8885	1188.46	2.0182	0.8246	0.7961	1227.49	2.0192	0.7350	0.8504	1064.68
375	2.0230	0.7054	0.8775	1188.88	2.0189	0.8416	0.7859	1227.89	2.0202	0.7333	0.8513	1065.23
400	2.0235	0.7305	0.8627	1189.15	2.0196	0.8538	0.7786	1228.30	2.0211	0.7383	0.8482	1065.70
450	2.0249	0.7777	0.8351	1189.99	2.0211	0.8699	0.7691	1229.20	2.0228	0.7606	0.8342	1066.58
500	2.0272	0.8032	0.8201	1191.36	2.0226	0.8796	0.7633	1230.13	2.0244	0.7796	0.8223	1067.43
550	2.0251	0.8300	0.7921	1190.11	2.0241	0.8883	0.7581	1231.04	2.0258	0.8143	0.8012	1068.20
600	2.0267	0.8535	0.7780	1191.04	2.0255	0.8960	0.7535	1231.89	2.0268	0.9038	0.7490	1068.68
650	2.0282	0.8684	0.7692	1191.95	2.0270	0.8993	0.7515	1232.79	2.0291	0.9233	0.7381	1069.92
700	2.0297	0.8774	0.7638	1192.81	2.0284	0.9030	0.7492	1233.66	2.0308	0.9375	0.7300	1070.82
750	2.0311	0.8840	0.7598	1193.65	2.0298	0.9062	0.7472	1234.53	2.0321	0.9469	0.7246	1071.49
800	2.0322	0.8813	0.7611	1194.29	2.0315	0.8973	0.7520	1235.52	2.0337	0.9450	0.7255	1072.33
850	2.0332	0.8779	0.7628	1194.89	2.0329	0.8832	0.7597	1236.39	2.0353	0.9424	0.7266	1073.15
900	2.0347	0.8750	0.7642	1195.75	2.0338	0.8760	0.7636	1236.94	2.0366	0.9445	0.7252	1073.86
950	2.0365	0.8706	0.7665	1196.83	2.0353	0.8764	0.7631	1237.84	2.0381	0.9519	0.7209	1074.65
1000	2.0381	0.8709	0.7662	1197.76	2.0364	0.8826	0.7593	1238.53	2.0391	0.9596	0.7165	1075.18
1050	2.0396	0.8702	0.7664	1198.64	2.0375	0.8895	0.7552	1239.23	2.0402	0.9636	0.7140	1075.79
1100	2.0410	0.8696	0.7665	1199.44	2.0388	0.8950	0.7518	1239.98	2.0415	0.9656	0.7127	1076.47
1150	2.0423	0.8697	0.7662	1200.20	2.0400	0.8971	0.7504	1240.70	2.0430	0.9661	0.7121	1077.22
1200	2.0436	0.8700	0.7657	1200.99	2.0413	0.8998	0.7486	1241.49	2.0444	0.9667	0.7115	1078.00
1250	2.0450	0.8700	0.7656	1201.83	2.0427	0.9014	0.7475	1242.35	2.0459	0.9671	0.7110	1078.78
1300	2.0463	0.8710	0.7647	1202.55	2.0439	0.9028	0.7464	1243.12	2.0473	0.9667	0.7110	1079.48
1350	2.0474	0.8717	0.7640	1203.19	2.0452	0.9030	0.7461	1243.89	2.0484	0.9673	0.7103	1080.08
1400	2.0486	0.8723	0.7634	1203.92	2.0465	0.9051	0.7447	1244.65	2.0498	0.9664	0.7105	1080.84
1450	2.0498	0.8731	0.7627	1204.64	2.0478	0.9062	0.7438	1245.46	2.0512	0.9661	0.7104	1081.55
1500	2.0509	0.8753	0.7611	1205.26	2.0490	0.9067	0.7433	1246.20	2.0522	0.9668	0.7097	1082.11
1550	2.0518	0.8766	0.7601	1205.80	2.0501	0.9070	0.7429	1246.85	2.0531	0.9670	0.7093	1082.56
1600	2.0531	0.8792	0.7584	1206.57	2.0516	0.9057	0.7434	1247.77	2.0544	0.9674	0.7088	1083.24
1650	2.0541	0.8810	0.7571	1207.14	2.0526	0.9053	0.7433	1248.36	2.0553	0.9674	0.7084	1083.70
1700	2.0551	0.8816	0.7565	1207.76	2.0537	0.9049	0.7433	1249.03	2.0565	0.9683	0.7076	1084.34
1750	2.0562	0.8845	0.7545	1208.40	2.0548	0.9052	0.7428	1249.71	2.0576	0.9684	0.7072	1084.95
1800	2.0571	0.8870	0.7528	1208.89	2.0556	0.9055	0.7423	1250.23	2.0585	0.9694	0.7064	1085.44
1850	2.0581	0.8883	0.7518	1209.49	2.0567	0.9052	0.7423	1250.89	2.0597	0.9693	0.7061	1086.03
1900	2.0591	0.8876	0.7520	1210.12	2.0579	0.9061	0.7415	1251.61	2.0608	0.9672	0.7069	1086.63
1950	2.0596	0.8866	0.7522	1210.41	2.0586	0.9081	0.7400	1252.04	2.0614	0.9660	0.7072	1086.95
2000	2.0608	0.8910	0.7494	1211.09	2.0597	0.9101	0.7386	1252.71	2.0630	0.9692	0.7052	1087.78

Table A2. Optical properties retrieved for the JSC Mars-1, MGS-1, and MMS-2 M size fractions using the hexahedra model.

$\lambda(\text{nm})$	JSC Mars-1 M				MGS-1 M				MMS-2 M			
	$\langle Q_{ext} \rangle$	$\langle \omega \rangle$	$\langle g \rangle$	$\langle \sigma_{ext} \rangle$	$\langle Q_{ext} \rangle$	$\langle \omega \rangle$	$\langle g \rangle$	$\langle \sigma_{ext} \rangle$	$\langle Q_{ext} \rangle$	$\langle \omega \rangle$	$\langle g \rangle$	$\langle \sigma_{ext} \rangle$
200	2.0745	0.8948	0.7596	6.2461	2.1157	0.9625	0.7091	2.0319	2.0531	0.9212	0.7332	13.4959
225	2.0826	0.8931	0.7603	6.2705	2.1373	0.9610	0.7116	2.0526	2.0582	0.9197	0.7328	13.5292
250	2.0937	0.9022	0.7558	6.3038	2.1592	0.9634	0.7123	2.0737	2.0632	0.9211	0.7310	13.5622
275	2.1063	0.9053	0.7546	6.3418	2.1804	0.9682	0.7121	2.0941	2.0679	0.9255	0.7275	13.5934
300	2.1190	0.9161	0.7499	6.3799	2.1997	0.9731	0.7119	2.1125	2.0732	0.9309	0.7237	13.6281
325	2.1323	0.9222	0.7476	6.4200	2.2164	0.9769	0.7118	2.1286	2.0790	0.9361	0.7200	13.6663
350	2.1459	0.9347	0.7422	6.4609	2.2294	0.9808	0.7116	2.1411	2.0843	0.9381	0.7181	13.7008
375	2.1573	0.9427	0.7394	6.4953	2.2398	0.9834	0.7118	2.1511	2.0901	0.9377	0.7178	13.7388
400	2.1688	0.9522	0.7356	6.5298	2.2462	0.9852	0.7121	2.1572	2.0954	0.9401	0.7158	13.7741
450	2.1902	0.9659	0.7314	6.5942	2.2492	0.9873	0.7128	2.1601	2.1065	0.9488	0.7106	13.8471
500	2.2064	0.9718	0.7311	6.6431	2.2404	0.9885	0.7132	2.1517	2.1182	0.9555	0.7069	13.9237
550	2.2122	0.9772	0.7058	6.6606	2.2226	0.9895	0.7127	2.1346	2.1305	0.9658	0.7016	14.0047
600	2.2265	0.9815	0.7050	6.7036	2.1975	0.9903	0.7116	2.1105	2.1438	0.9855	0.6918	14.0924
650	2.2374	0.9840	0.7060	6.7366	2.1676	0.9905	0.7111	2.0817	2.1575	0.9888	0.6916	14.1819
700	2.2458	0.9855	0.7064	6.7616	2.1349	0.9908	0.7097	2.0504	2.1723	0.9912	0.6913	14.2795
750	2.2509	0.9864	0.7074	6.7770	2.1004	0.9911	0.7085	2.0172	2.1867	0.9927	0.6922	14.3739
800	2.2539	0.9861	0.7087	6.7860	2.0655	0.9899	0.7078	1.9837	2.2019	0.9925	0.6940	14.4743
850	2.2545	0.9856	0.7101	6.7879	2.0310	0.9880	0.7075	1.9506	2.2164	0.9922	0.6960	14.5694
900	2.2537	0.9852	0.7112	6.7855	1.9973	0.9869	0.7068	1.9182	2.2314	0.9925	0.6976	14.6682
950	2.2511	0.9845	0.7128	6.7778	1.9647	0.9868	0.7062	1.8869	2.2454	0.9937	0.6994	14.7597
1000	2.2476	0.9846	0.7133	6.7672	1.9337	0.9875	0.7047	1.8572	2.2595	0.9948	0.7003	14.8526
1050	2.2427	0.9844	0.7146	6.7525	1.9041	0.9882	0.7041	1.8287	2.2725	0.9953	0.7025	14.9380
1100	2.2371	0.9843	0.7155	6.7356	1.8761	0.9888	0.7035	1.8018	2.2849	0.9957	0.7043	15.0195
1150	2.2306	0.9843	0.7162	6.7158	1.8495	0.9889	0.7030	1.7762	2.2966	0.9958	0.7060	15.0965
1200	2.2231	0.9844	0.7173	6.6933	1.8242	0.9891	0.7031	1.7519	2.3070	0.9959	0.7082	15.1645
1250	2.2150	0.9843	0.7181	6.6690	1.8003	0.9892	0.7030	1.7290	2.3164	0.9959	0.7099	15.2267
1300	2.2062	0.9844	0.7187	6.6425	1.7776	0.9893	0.7030	1.7072	2.3249	0.9959	0.7116	15.2822
1350	2.1967	0.9845	0.7197	6.6138	1.7560	0.9892	0.7035	1.6864	2.3320	0.9960	0.7134	15.3291
1400	2.1865	0.9845	0.7205	6.5831	1.7354	0.9894	0.7039	1.6666	2.3378	0.9959	0.7153	15.3674
1450	2.1756	0.9846	0.7210	6.5502	1.7155	0.9894	0.7041	1.6476	2.3425	0.9959	0.7165	15.3983
1500	2.1640	0.9849	0.7216	6.5154	1.6963	0.9894	0.7047	1.6292	2.3461	0.9960	0.7180	15.4218
1550	2.1518	0.9850	0.7224	6.4786	1.6779	0.9893	0.7055	1.6115	2.3482	0.9960	0.7196	15.4356
1600	2.1391	0.9854	0.7229	6.4405	1.6602	0.9891	0.7062	1.5944	2.3492	0.9960	0.7208	15.4425
1650	2.1256	0.9856	0.7232	6.3998	1.6427	0.9889	0.7067	1.5777	2.3489	0.9961	0.7218	15.4401
1700	2.1115	0.9856	0.7237	6.3575	1.6257	0.9888	0.7074	1.5613	2.3474	0.9962	0.7229	15.4305
1750	2.0971	0.9860	0.7242	6.3140	1.6092	0.9887	0.7082	1.5454	2.3448	0.9962	0.7241	15.4132
1800	2.0821	0.9863	0.7246	6.2690	1.5930	0.9887	0.7090	1.5299	2.3410	0.9963	0.7251	15.3885
1850	2.0664	0.9864	0.7248	6.2216	1.5768	0.9886	0.7095	1.5144	2.3360	0.9963	0.7258	15.3552
1900	2.0502	0.9862	0.7251	6.1728	1.5610	0.9886	0.7100	1.4992	2.3298	0.9960	0.7266	15.3146
1950	2.0335	0.9860	0.7255	6.1224	1.5453	0.9888	0.7106	1.4841	2.3226	0.9959	0.7274	15.2672
2000	2.0167	0.9866	0.7256	6.0720	1.5299	0.9890	0.7113	1.4693	2.3147	0.9963	0.7280	15.2156

This paper has been typeset from a $\text{\TeX}/\text{\LaTeX}$ file prepared by the author.